Materials Science and Engineering B 295 (2023) 116571

Contents lists available at ScienceDirect

Materials Science & Engineering B

journal homepage: www.elsevier.com/locate/mseb

# Correlation of phase composition, magnetic properties and hyperthermia efficiency of silica-coated FeCo nanoparticles for therapeutic applications

Pham Hoai Linh [a,b], Julia Fedotova [c], Svetlana Vorobyova [d], Luu Huu Nguyen [e,f,*], Tran Thi Huong [a], Hong Nhung Nguyen [a], Thi Ngoc Anh Nguyen [a], Anh Son Hoang [a], Quang Anh Nguyen [g], Uladzislaw Gumiennik [h], Artem Konakov [d], Maxim Bushinskij [i], Pawel Zukowski [j], Tomasz N. Koltunowicz [j,*]

[a] Institute of Materials Science, Vietnam Academy of Science and Technology, 18, Hoang Quoc Viet Str., Cau Giay 1000000, Hanoi, Vietnam
[b] Graduate University of Science and Technology, Vietnam Academy of Science and Technology, 18, Hoang Quoc Viet Str., Cau Giay 1000000, Hanoi, Vietnam
[c] Institute for Nuclear Problems of Belarusian State University, 11, Bobrujskaya Str., 220006 Minsk, Belarus
[d] Research Institute for Physical Chemical Problems of the Belarusian State University, 14, Leningradskaya Str., 220006 Minsk, Belarus
[e] Laboratory of Magnetism and Magnetic Materials, Science and Technology Advanced Institute, Van Lang University, No 69/68 Dang Thuy Tram Street, Ward 13, Binh Thanh District, Ho Chi Minh City 700000, Vietnam
[f] Faculty of Applied Technology, School of Technology, Van Lang University, No. 69/68 Dang Thuy Tram Street, Ward 13, Binh Thanh District, Ho Chi Minh City 700000, Vietnam
[g] Faculty of Mechanical Engineering, University of Transport Technology, 54, Trieu Khuc Str., Thanh Xuan, 100000 Hanoi, Vietnam
[h] AGH University of Science and Technology, Faculty of Physics and Applied Computer Science, Department of Solid State Physics, 19, Reymonta Str., 30-059 Krakow, Poland
[i] Scientific-Practical Materials Research Centre NAS of Belarus, 19, P. Brovki Str., 220072 Minsk, Belarus
[j] Lublin University of Technology, Department of Electrical Devices and High Voltage Technology, 38A, Nadbystrzycka Str., 20-618 Lublin, Poland

ARTICLE INFO

*Keywords:*
FeCo alloy
Core–shell nanoparticles
Mössbauer spectroscopy
Magnetic induction heating
Drug loading
In-vitro toxicity

ABSTRACT

The local atomic order, magnetic properties, hyperthermia efficiency, drug loading capacity and in-vitro cytotoxicity are investigated for the core–shell $(Fe_{25}Co_{75})_x(SiO_2)_{100-x}$ ($70 \leq x \leq 100$, wt.%) nanoparticles (NPs) sintered by the metals co-precipitation followed with $SiO_2$ TEOS deposition. Electron microscopy reveal the formation of nearly spherical structures with medium diameter from 80 nm to 220 nm containing 20–50 nm cores identified by XRD as α-FeCo bcc alloy. Mössbauer spectra and magnetometry reflects the formation of magnetically-interacting net of single-domain FeCo cores with broad size distribution. Observed decrease in magnetization ($M_S$) and effective magnetic anisotropy ($K_{eff}$) for NPs with × is the consequence of the increasing thickness of the $SiO_2$ shells. Calculations indicate that there is an optimal thickness δ of $SiO_2$ shells ranging between 90 ÷ 120 nm for the highest value of specific absorption rate (SAR) originating from their effect on $K_{eff}$ values. Experimentally proved that SAR has the highest value for $(FeCo)_{80}(SiO_2)_{20}$ NPs in correlation with the Linear Response Theory approach. High drug loading capacity (up to 98 %) and low in-vitro cytotoxicity ($IC_{50}$ index below 230 μg/ml) experimentally proved for $(FeCo)_x(SiO_2)_{100-x}$ NPs make them perfect candidates for designing smart drug delivery systems.

* Corresponding authors at: Laboratory of Magnetism and Magnetic Materials, Science and Technology Advanced Institute, Van Lang University, No 69/68 Dang Thuy Tram Street, Ward 13, Binh Thanh District, Ho Chi Minh City 700000, Vietnam (L.H. Nguyen); Department of Electrical Devices and High Voltage Technology, Lublin University of Technology, 38A, Nadbystrzycka Street, 20-618 Lublin, Poland (T.N. Kotunowicz).

*E-mail addresses:* linhph@ims.vast.ac.vn (P. Hoai Linh), Julia@hep.by (J. Fedotova), Vorobyova@bsu.by (S. Vorobyova), luuhuunguyen@vlu.edu.vn (L. Huu Nguyen), anhntn@ims.vast.ac.vn (T. Thi Huong), huongtt@ims.vast.ac.vn (H. Nhung Nguyen), nhungnh@ims.vast.ac.vn (T. Ngoc Anh Nguyen), sonha@ims.vast.ac.vn (A. Son Hoang), quanganh_1967@yahoo.com.vn (Q. Anh Nguyen), konakov@bsu.by (A. Konakov), p.zhukowski@pollub.pl (P. Zukowski), t.koltunowicz@pollub.pl (T.N. Koltunowicz).

https://doi.org/10.1016/j.mseb.2023.116571
Received 24 January 2023; Received in revised form 3 May 2023; Accepted 10 May 2023
Available online 18 May 2023

## 1. Introduction

Recent advances in nanomedicine definitely prove great perspectives of metallic (Fe, Co) and metallic oxides ($Fe_3O_4$, $CoFe_2O_4$, Ni-Zn ferrites) nanoparticles (NPs) in such a rapidly growing field as theranostics that combines therapeutics and imaging capabilities [1–7]. Such biomedical application requires a combination of specific functional properties (high magnetic moment, high drug-loading capacity, high SAR, biocompatibility) in order to design proper NPs-based nanodevices. For this reason, NPs of FeCo alloy possessing very high value of saturation magnetization $M_S$ [1] seem to be excellent choices because this is the key parameter for high SAR value as well as for sensitivity of smart drug delivery nanodevices to the external magnetic field. Especially, FeCo alloy NPs with high saturation magnetization will lead to large thermal energy, which improves the ability to kill tumor cells in hyperthermia. For example, J. Alonso et. al found a high value of SAR (~1500 W/g) of FeCo NPs at a field 300Oe and 310 kHz [8]. L.-M. Lacroix et. al demonstrated that 14.2 nm FeCo has high losses (1.5 mJ/g) in hyperthermia [3]. Although FeCo NPs in their pristine state are toxic for living cells and are typically subject to undesirable surface oxidation, both disadvantages could be easily overcome by coverage with $SiO_2$ or $Al_2O_3$ layers (shells) [9,10]. Coating layers of $SiO_2$ are well known as the most suitable candidates for drug delivery application because of their appropriate properties such as chemical stability, high specific area, biocompatibility, ability to easily functionalization with biological objects (DNA, enzyme…) [10]. For instance, the improvement of the saturation magnetization for the core-shells NPs with $SiO_2$ shells was found in the works of et. al [11,12]. In addition, H. Das et. al demonstrated that $MgFe_2O_4/SiO_2$ core–shell NPs are a promising heating agent in hyperthermia [13]. Similarly, the role of the $SiO_2$ layer in improving the applicability of core NPs is also found in the works of M. Talaei et. al [14], M. Tajabadi [15]. It is reported in [16] that the value of saturation magnetization of $(FeCo)_x(SiO_2)_{100-x}$ core–shell NPs was higher than 100 emu/g. Thus, all mentioned results indicate that the combination of FeCo (alloy) NPs with the $SiO_2$ layer in core–shell NPs is the promising approach to search an effective agent heating in hyperthermia. However, the effect of $SiO_2$ shells on the local atomic order in FeCo cores as well as their magnetic properties in correlation with the value of SAR for $(FeCo)_x(SiO_2)_{100-x}$ NPs has been not clarified. Therefore, this combination is still an open, and important issue. Additionally, porous $SiO_2$ shells are well known as an outstanding platform for drug delivery carriers due to their pore characterization, which can be loaded with therapeutic drugs and then capped with specific gatekeeper molecules [11,12,17]. The combination of FeCo NPs cores and the high drug loading capacity of the $SiO_2$ shell allows us to design smart controlled drug delivery systems [18]. These core–shell NPs take advantage of FeCo cores magnetic response with the heat generation in the alternating magnetic field and the high drug loading ability of mesoporous $SiO_2$ shells for the combination of hyperthermia and drug delivery. To the best of our knowledge, application of $FeCo@SiO_2$ NPs used for smart drug delivery have not been examined in detail. Therefore, research to explore the role of $SiO_2$ contents in the drug loading efficacy of $FeCo@SiO_2$ NPs is still a matter of concern.

In the present work, for the first time a complementary study is carried out that reveals correlation of magneto-structural state of the core–shell $(FeCo)_x(SiO_2)_{100-x}$ NPs with the efficacy of their application in hyperthermia in combination with characterization of their biomedical properties (drug loading capacity and in vitro cytotoxicity).

For study of phase composition, we apply X-ray diffraction (XRD) and $^{57}$Fe Mössbauer spectroscopy probing local atomic states of Fe ions inside NPs that makes is advantageous technique to investigate oxidation of NPs with respect to other techniques of structural analysis. Magnetic state of NPs is studied by external magnetic field and temperature (under FC-ZFC protocols) dependencies of magnetization. The therapeutic applications of the synthesized samples were studied through investigations of magnetic hyperthermia properties and Doxorubicin (DOX) drug loading capacity. The values of specific absorption rate (SAR) for $(FeCo)_x(SiO_2)_{100-x}$ NPs are calculated and experimentally studied. The experimental proof is supported with modelling results of correlation between magnetic anisotropy and inductive magnetic heating of $(Fe_{25}Co_{75})_x(SiO_2)_{100-x}$ NPs, elucidation of the optimal composition of NPs, simultaneously evidencing appropriate values of biomedical characteristics. All this put together makes studied NPs very prospective for designing new biocompatible nanodevices for effective application in targeted drug delivery and hyperthermia therapy.

## 2. Experimental

### 2.1. Preparation of the samples

#### 2.1.1. Materials

Cobalt chloride hexahydrate $CoCl_2{\cdot}6H_2O$ 98.0 % (Vecton, Russia), iron sulphate heptahydrate $FeSO_4{\cdot}7H_2O$ > 98.0 % (Vecton, Russia), sodium borohydride 98 %, tetraethyl orthosilicate (TEOS) 99.9 % (Ecos-1, Russia), isopropanol 99.9 % (Ecos-1), ammonium hydroxide 25 % (Analytcomplect) were used as received. Distilled water was used for all the preparations.

#### 2.1.2. Synthesis of $Fe_{25}Co_{75}$ and $(FeCo)_x(SiO_2)_{100-x}$ NPs

The core–shell $(Fe_{25}Co_{75})_x(SiO_2)_{100-x}$ ($70 \leq x \leq 100$, wt.%) NPs are prepared by two stages including co-precipitation of FeCo NPs from aqua solutions with further deposition of $SiO_2$ shells onto FeCo NPs by TEOS hydrolysis. The composition of FeCo cores is chosen based on the magnetometry results on $Fe_xCo_{100-x}$ NPs ($25 \leq x \leq 75$, wt.%) confirming the highest value of saturation magnetization $M_S$ (up to 63.5 emu/g) for $Fe_{25}Co_{75}$ [19,20].

FeCo NPs are prepared by chemical deposition from aqua solutions. For that, 5.0 g of iron (II) sulfate heptahydrate and 12.8 g of cobalt chloride hexahydrate were dissolved in 350 ml of the distilled water and deaerated using the Schlenk line. Then the alkaline solution of sodium borohydrate, obtained by dissolving 1.8 g NaOH and 7.2 g $NaBH_4$ in 150 ml of the distilled water, was added drop by drop to the solution of iron (II) sulfate heptahydrate and cobalt chloride hexahydrate under stirring. The obtained sediment was washed with distilled water and dried at ambient temperature over $P_2O_5$. All procedures were carried out in Ar atmosphere.

Then $SiO_2$ is deposited onto FeCo NPs by TEOS hydrolysis. For this purpose, 2.5 g of FeCo powder were dispersed in 50 ml isopropanol using ultrasonic dispersant for 30 min and TEOS was added to prepared FeCo dispersion. The quantities of TEOS varied from 1.9 to 5.6 ml. The obtained mixture is additionally dispersed in an ultrasonic dispersant for 1 h. After that concentrated ammonium solution was added to the prepared dispersion and was dispersed in an ultrasonic dispersant for 1 h. The $(FeCo)_x(SiO_2)_{100-x}$ NPs are separated from the dispersion by centrifugation and the resulting powder was dried in vacuum.

### 2.2. Characterization methods

The morphology and structure of NPs are investigated by scanning (SEM, S-4800 Hitachi) and transmission electron microscopes (TEM, JEM-2100Plus, JEOL). The phase composition of NPs is analyzed by X-ray diffraction (XRD, Bruker D8 Advance diffractometer) in Co-Kα ($\lambda$ = 1.79026 Å) radiation and in the range of angles 2θ between 20° and 80° with a step size of 0.02. Local atomic states in NPs are studied by $^{57}$Fe Mössbauer spectroscopy in the transmission geometry using a conventional constant acceleration type spectrometer (Janis) with a 30 mCi $^{57}$Co/Rh source at temperatures 300 K and 5 K. The spectra were analyzed with the RECOIL software presuming distributions of hyperfine field ($H_{hf}$), isomer shift (δ) and quadrupole splitting (Δ) [21]. Magnetization curves $M(H)$ were studied by vibrating sample magnetometer (VSM-MPMS, Quantum Design) in the temperature range from 2 up to

300 K and in magnetic fields $H$ up to 80 kOe. Temperature dependencies of magnetization $M(T)$ are measured in zero-field cooling (ZFC) and field-cooling (FC, $H = 1000$ Oe) modes.

FTIR spectroscopy (FTIR-GBC Cintra 40 Nicolet Nexus 670 FTIR) with the wavenumber ranging from 400 $cm^{-1}$ to 4000 $cm^{-1}$ is carried out to investigate the chemical structures of the synthesized samples. The Brunauer-Emmett-Teller (BET) specific surface area and the Barrett-Joyner-Halenda (BJH) pore size distribution of the samples were determined by nitrogen adsorption at 77 K using a Micromeritics 3Flex Surface Characterization Analyzer.

DLS measurements are performed by Zetasizer Nano ZS device (Malvern Instruments) determining the hydrodynamic size and polydispersity of the $(FeCo)_x(SiO_2)_{100-x}$ NPs. DLS experiments are conducted with a standard cuvette containing NPs (concentration of 0.5 mg/ml) dispersed in water at pH 7.

### 2.3. Magnetic heating experiments

The magnetic heating efficiency of $(FeCo)_x(SiO_2)_{100-x}$ NPs was investigated through the time dependence temperature curves by using a calorimetry measurement in an alternating magnetic field conducted by a commercially available UHF-20A Module. In each measurement, 1 ml of the magnetic solution (5 mg/ml in water) was used. Based on the heating curves, the SAR values were calculated according to the following equation [1]:

$$SAR\left(W.g^{-1}\right) = \frac{\sum C_i m_i}{m_M}\frac{dT}{dt} \quad (1)$$

where $C_i$ and $m_i$ are the specific heat capacity and mass of each component ($C_{FeCo} = 0.449$ $Jg^{-1}K^{-1}$ for Fe NPs, $C_{SiO2} = 0.680$ $Jg^{-1}K^{-1}$ and $C_{H2O} = 4.185$ J $Jg^{-1}K^{-1}$), $m$ is the concentration (mg mL1) of magnetic material in solution, and $dT/dt$ is the initial slope of the measured temperature $T$ rise curve with time $t$. In the experiments, the $T(t)$ curve can be described by the following equation:

$$T(t) = T_{initial} + \Delta T_{max}(1 - \exp(-t/\tau)) \quad (2)$$

where $\Delta T_{max}$ is the temperature difference between the initial and steady state, and $\tau$ is the time constant of the heating. $dT/dt = \Delta T_{max}/\tau$ is determined by fitting the experimental data to the expression (2).

### 2.4. The DOX loading experiment

Typically, 80 mg of the core–shell $(FeCo)_x(SiO_2)_{100-x}$ NPs were dispersed in 40 ml PBS solution containing DOX drug with the concentration of 200 ppm under the help of a magnetic stirring in the dark and kept for 48 h to achieve the absorption/desorption equilibrium. The DOX–loaded $(FeCo)_x(SiO_2)_{100-x}$ NPs are collected magnetically and washed with pure water several times and then dried at 25 °C in the oven. The unloaded DOX drug in the solution was determined by fluorescence spectroscopy at 591 nm. The drug loading efficiency (DLE) and drug loading capacity (DLC) of DOX in the $(FeCo)_x(SiO_2)_{100-x}$ NPs are calculated as follows:

$$DLE = \frac{C_t}{C0}.100\% \quad (3)$$

where $C_0$ is the initial concentration of DOX: $C_0 = 200$ ppm, $C_t$ is the concentration of DOX in NPs: $C_t = C_0$-$C_R$, $C_R$ is the concentration of free DOX in the solution after adsorption process:

$$DLC = \frac{m_D}{m}.100\%, \quad (4)$$

where $m_D$ is the mass of DOX loaded onto NPs: $m_D$ $m_o$-$m_R$, $m_0$ is the initial mass of DOX, $m_R$ is the mass of free DOX after the adsorption process. The concentration of DOX was estimated by fluorescence spectroscopy (FL) measurement at 591 nm through the calibration curve of the relationship between the FL intensity and DOX concentration (0.05, 0.1, 0.5, 1, 2.5, 5, 7.5, 10 ppm) (Figure S1).

### 2.5. In vitro toxicity experiments

Sulforhodamine B assays were performed to study the cytotoxicity experiment (a human liver cancer cell line) of $(FeCo)_x(SiO_2)_{100-x}$ NPs on HepG2 cells, the approach was described in detail in the previous study [22]. In this test, the solution containing the $(FeCo)_x(SiO_2)_{100-x}$ NPs with concentrations from 31.25 μg/ml to 1000 μg/ml was incubated with HepG2 cells for 48 h. The doxorubicin (Ebewe Pharma) was used as the control of the cytotoxic drug with the treated concentration from 0.079 μg/ml to 31.25 μg/ml. After the incubation time, cancer cells were fixed by trichloroacetic acid (10 %) for one hour at a temperature of 4 °C. Next, this solution was washed with water, and dried in air. The 0.4 % (v/v) SRB was used to stain cellular proteins for ten minutes. The excess dye was removed by five times washing with 1 % (v/v) acetic acid. Finally, all plates were utterly dried in the air, and the bound-protein stain was solubilized with Tris Base (10 mM). The absorbance of samples was measured by a microplate reader (BioRad) at a fixed wavelength of 540 nm. Cell viability (CV) was computed using the following equation (5) as follows:

$$A\% = \frac{T - T_Z}{VH - T_Z} \quad (5)$$

where $T$, $T_z$, and $VH$ are the fluorescence densities of the well containing the $(FeCo)_x(SiO_2)_{100-x}$ NPs, culture medium without the cells, and control cells, respectively.

Statistical analysis was done using the GraphPad Prism software (version 5.04) with one-way ANOVA and $t$-test analyses. Assay in triplicates and data with P-value $< 0.05$ were considered significant.

## 3. Results and discussion

### 3.1. Morphology and phase composition

Typical SEM and TEM images for $(FeCo)_x(SiO_2)_{100-x}$ NPs are shown in Fig. 1 SEM images of the $(FeCo)_x(SiO_2)_{100-x}$ NPs reveal the ensemble of nearly spherical NPs of about 80–220 nm in size depending on the contribution of the $SiO_2$. Typical TEM image of samples (see the inset to Fig. 1d) shows that every NPs observed by SEM contains inside few fine grains. These grains appear as dark or dark-grey contrast with individual medium diameter $D \approx 20$–50 nm. Selected area electron diffraction (SAED) patterns reveal diffuse halo typical for nanosized or poorly-crystallized NPs.

The size distribution of $(FeCo)_x(SiO_2)_{100-x}$ NPs suspended in the aqueous medium was investigated through DLS measurements (Fig. 2a). It is evidenced that the average hydrodynamic size $d$ of nanoclusters in an aqueous solution increases with the $SiO_2$ content in good correlation with SEM results in Fig. 1a-c. Fig. 2a shows that $(FeCo)_{80}(SiO_2)_{20}$ NPs reveal the best monodispersity and the value of average size $d = 152$ nm which is the optimum for in vivo drug delivery, as reported by the previous study [23]. Zeta potential was recorded to be −31.28 mV, −25.39 mV and –22.94 mV for the samples with × = 10, 20 and 30, respectively. Zeta potential exhibited that the core–shell NPs have a negative charge revealing the existence of $OH^-$ on their surface that helps them well dispersed in the aqueous medium.

Fig. 2b displays the XRD patterns of $(FeCo)_x(SiO_2)_{100-x}$ NPs. It is seen that the reflections at $2\Theta \approx 53°$ and $2\Theta \approx 28°$, correspond to *bcc* α-FeCo (1 1 0) and amorphous $SiO_2$ phases, correspondingly [19]. The broadening of the α-FeCo diffraction peak with half-width on half-medium of about 10°that is much beyond the instrumental linewidth of the diffractometer should be assigned to the disordered (amorphous) state of NPs in correlation with SAED in the inset to Fig. 1d. It is worth noticing that contrary to the case of uncoated FeCo cores that reveal a

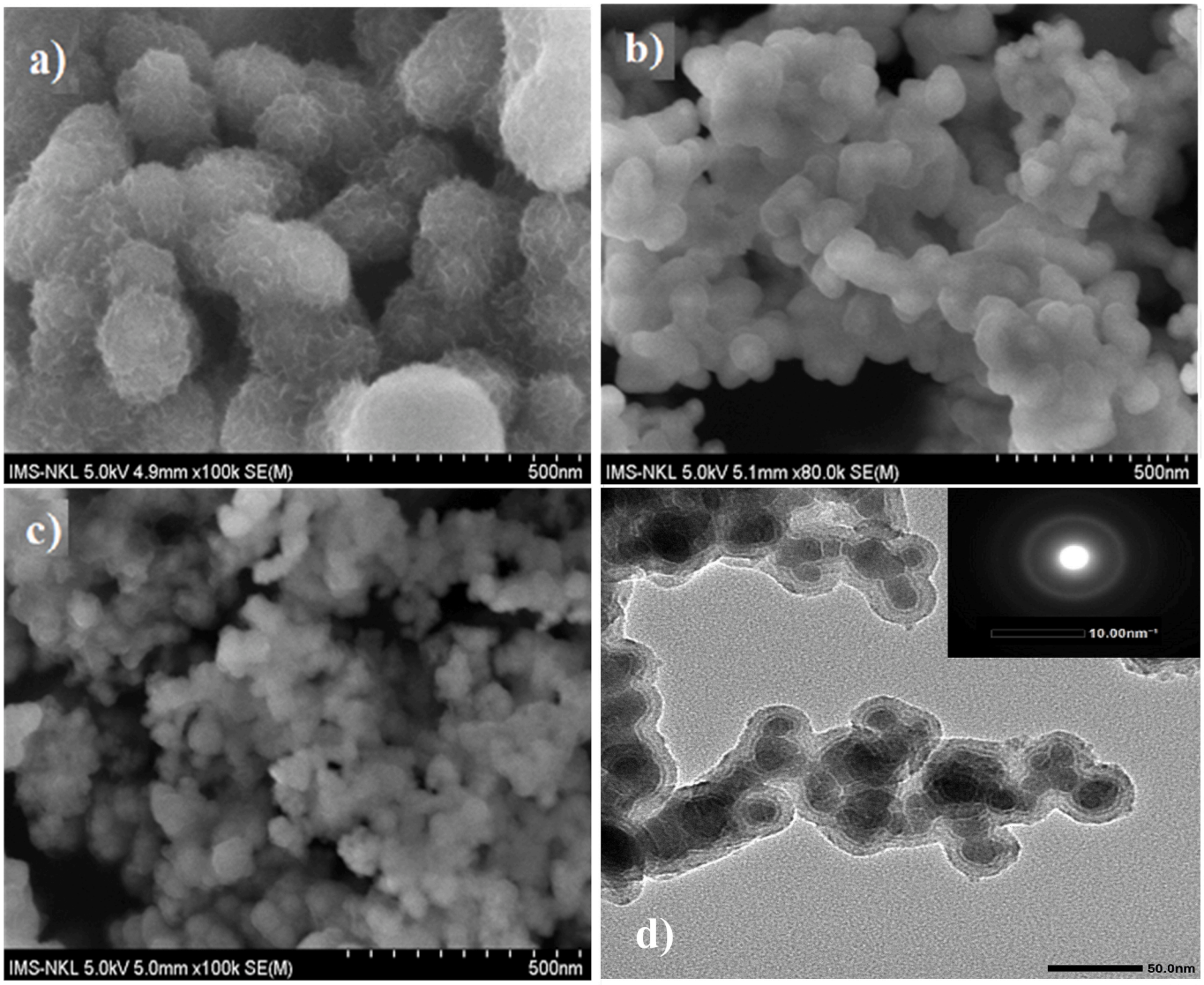


**Fig. 1.** SEM images of $(FeCo)_{70}(SiO_2)_{30}$ (a), $(FeCo)_{80}(SiO_2)_{20}$ (b), $(FeCo)_{90}(SiO_2)_{10}$ (c) NPs. Typical TEM image of $(FeCo)_{80}(SiO_2)_{20}$ NPs (d); the insert shows electron diffraction pattern of $(FeCo)_{70}(SiO_2)_{30}$ NPs.

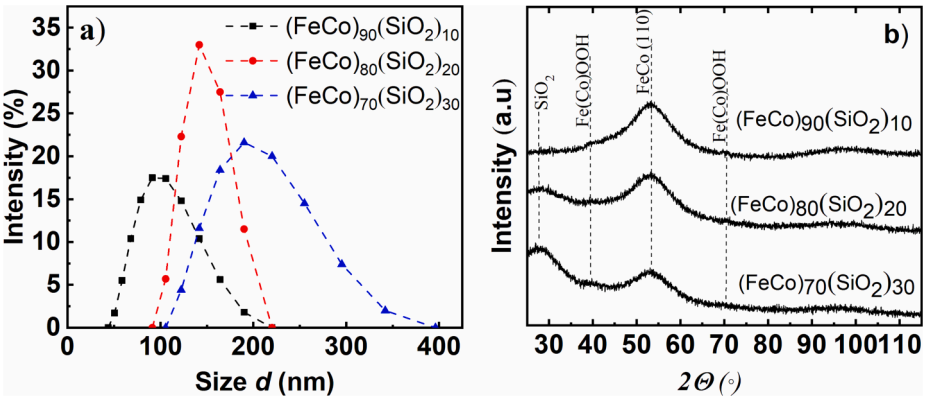


**Fig. 2.** Hydrodynamic size $d$ distribution (a) and XRD patterns (b) of $(FeCo)_x(SiO_2)_{100-x}$ NPs.

significant contribution of Fe(Co) hydroxide phase [19], their amount in core–shell $(FeCo)_x(SiO_2)_{100-x}$ NPs seems to be less pronounced (see Fig. 2b). So far, one can conclude that $SiO_2$ shells formed around α-FeCo cores preserve them from oxidation which is favorable for targeted drug delivery.

As presented in Fig. 3, $^{57}$Fe Mössbauer spectra for $(FeCo)_x(SiO_2)_{100-x}$ NPs recorded at $T = 5$–300 K reveal magnetically-collapsed sextets with strongly broadened spectral lines in the whole $T$ range. Based on the

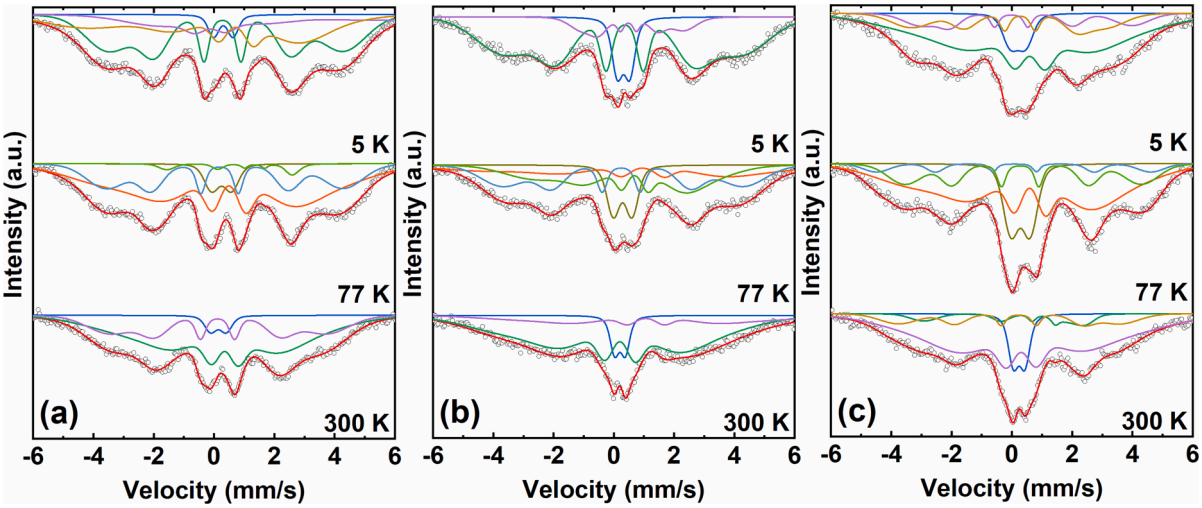


**Fig. 3.** Mossbauer spectra of $(FeCo)_{90}(SiO_2)_{10}$ (a), $(FeCo)_{80}(SiO_2)_{20}$ (b), $(FeCo)_{70}(SiO_2)_{30}$ (c) NPs recorded at $T = 5$–300 K.

interpretation of XRD patterns in Fig. 2b all the spectra were approximated assuming the dominating contribution of α-FeCo alloy with some amount of hydroxide Co(Fe)OH phase. In accordance with the approach proposed in [24] the number of subspectra was chosen to be the minimum required in order to obtain a good fit with $\chi^2 \approx 0.7$. So far, the best fit for all studied compositions was obtained presuming superposition of

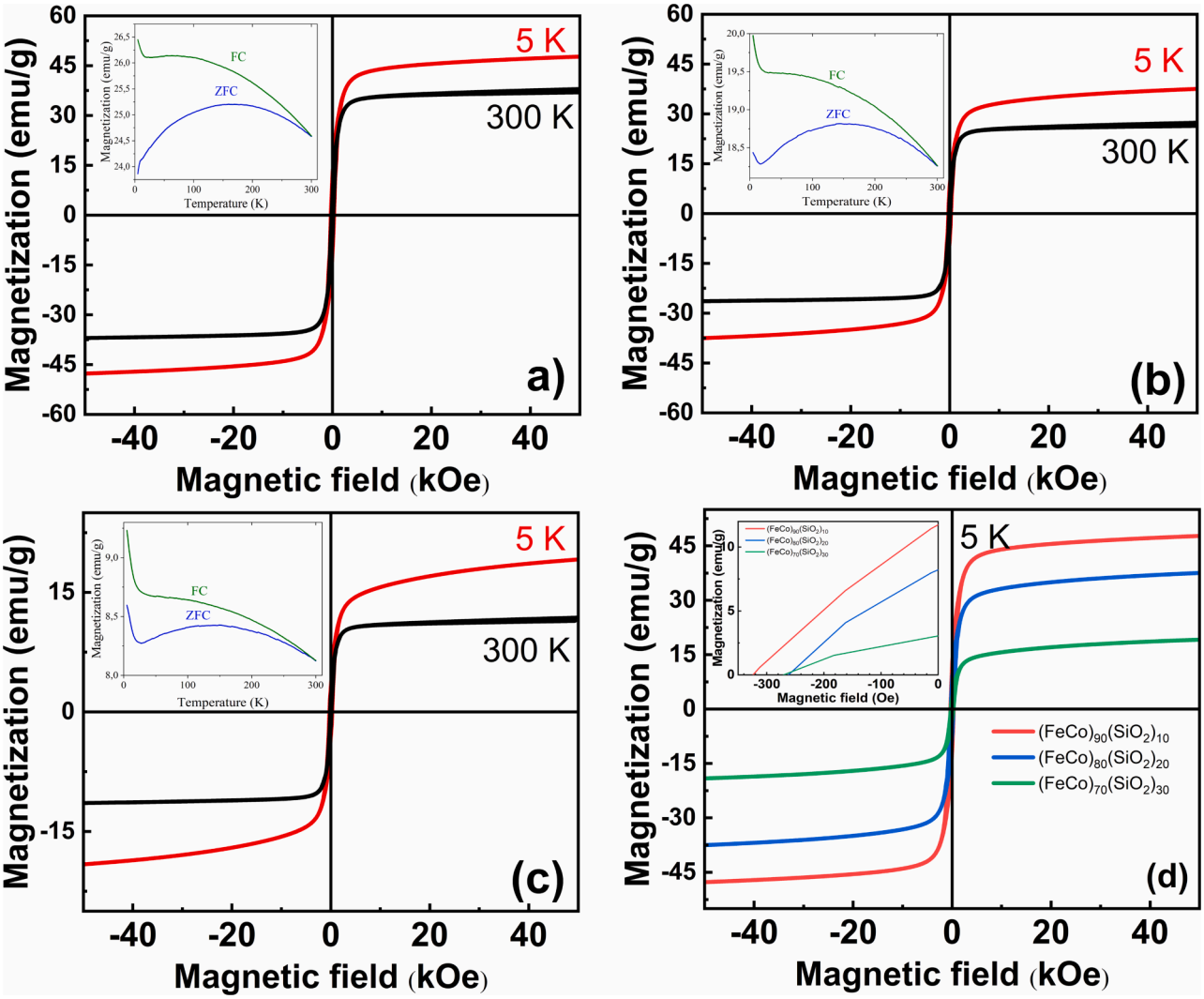


**Fig. 4.** $M(H)$ curves of $(FeCo)_{90}(SiO_2)_{10}$ NPs (a), $(FeCo)_{80}(SiO_2)_{20}$ NPs (b), $(FeCo)_{70}(SiO_2)_{30}$ NPs (c) (the inserts show $M(T)$ curves recorded under FC ($H = 1000$ Oe) and ZFC protocols) and $M(H)$ curves for the $(FeCo)_x(SiO_2)_{100-x}$ NPs (d) at 5 K.

four subspectra – two quadrupole doublets $Fe^{3+}$ and $Fe^{2+}$, and two magnetic sextets with large $H_{hf}$ distribution – with parameters and relative contributions ($A$) varying as a function of $T$ and NPs composition. In accordance with the fitting for uncoated $Fe_{25}Co_{75}$ NPs reported in [19], two central doublets $Fe^{3+}$ ($\delta = 0.35$–$0.46$ mm/s, $\Delta = 0.54$ mm/s) and $Fe^{2+}$ ($\delta \approx 1$ mm/s, $\Delta \approx 2.5$ mm/s) are assigned to Co(Fe)OH hydroxide and wüstite-type $Co^{2+}_{1-y}Fe^{2+}{}_yO$ phases, correspondingly. Magnetically-collapsed part of the spectra was fitted with the superposition of two sextets with medium values of $H_{hf1} \approx 15$–$19$ T and $H_{hf2} \approx 20$–$23$ T at $T = 300$ K which should be assigned to agglomerations of magnetically interacting FeCo cores. Temperature evolution of the values of $H_{hf1}$ and $H_{hf2}$ reveals the tendency to increase with $T$ decrease ($H_{hf1} \approx 18$–$21$ T and $H_{hf2} \approx 24$–$25$ T at $T = 5$ K). It is associated with the decreasing effect of thermally-induced magnetic moment fluctuations typically observed for NPs with a medium size around tens nm. The comparison of hyperfine parameters of subspectra extracted from approximation clearly reveal that no traces of ferrite phases generally characterized sextets with values of $H_{hf}$ ranging between 32 and 52 T are observed in the spectra [25].

Fitting of the spectra reveals that the largest contribution of surface hydroxide Co(Fe)OH phase (up to 35 %) is observed for NPs of $(FeCo)_{70}(SiO_2)_{30}$ composition. At the same time, it abruptly decreases up to 2–5 % for $(FeCo)_{80}(SiO_2)_{20}$ and $(FeCo)_{90}(SiO_2)_{10}$ NPs. This possibly correlates with the peculiarities of $SiO_2$ shells deposition over FeCo cores promoting the formation of Co(Fe)OH. It is worth noticing also that the values of $H_{hf1}$ and $H_{hf2}$ extracted from fitted Mössbauer spectra generally are not affected by $SiO_2$ contribution in $(FeCo)_x(SiO_2)_{100-x}$ NPs that reflects quite stable local atomic order in pure FeCo cores.

### 3.2. Magnetic properties

Magnetic properties of the core–shell NPs were studied by $M(H)$ and $M(T)$ curves recorded under FC and ZFC regimes for $(FeCo)_x(SiO_2)_{100-x}$ NPs are shown in Fig. 4. The values of magnetization at maximum applied magnetic field $H = 5$ T ($M_{H=5T}$), coercive force ($H_C$), blocking temperature ($T_B$), bifurcation temperature ($T_b$) extracted from the $M(H)$ and $M(T)$ curves are summarized in Table 1. The values of $M$ ranging between 47.7 and 19.1 emu/g at $T = 5$ K are close to those previously observed for FeCo NPs [1,18] but are higher than typically detected for Co ferrites NPs with close Fe:Co ratio [25].

The behavior of $M(H)$ curves for all studied compositions is quite typical for agglomerations of nanosized core–shell NPs as it reveals the increase of $M_{H=5T}$ value with $T$ decreasing from 300 K to 5 K. For all × values, FC-ZFC curves reveal a quite broad maximum on ZFC curves. Also, a large discrepancy is observed between blocking temperature $T_B$ (138 K, 161 K and 170 K for × = 90, 80 and 70, correspondingly) defined as the maximum on ZFC curve, and bifurcation temperature $T_b \approx 300$ K between FC and ZFC curves (see Table 1). The combination of these two features evidences the formation of superferromagnetic ordering [2,26] of magnetically-interacting single-domain FeCo cores with broad size distribution. These data well correlate with broad $(FeCo)_x(SiO_2)_{100-x}$ NPs size distribution presented in Fig. 2a as well as the shape and temperature evolution of Mössbauer spectra in Fig. 3.

Fig. 4d shows the $M(H)$ curves and the zoom of their low field region recorded at $T = 5$ K for $(FeCo)_x(SiO_2)_{100-x}$ NPs. As evidenced from these curves and Table 1, $M_{H=5T}$ and $H_C$ values normally decrease with increasing in nonmagnetic $SiO_2$ shells contribution in NPs. At $T = 300$ K the tendency is generally the same with the exception of the uncovered FeCo NPs, demonstrating a low $M_{H=5T}$ value which can be attributed to large contribution of hydroxide Co(Fe)OH phase (>35 %) as reported in our previous study [19]. It is worth noticing, however, that the value of $M_s$ (38 emu/g) at × = 90 was larger than that of uncovered FeCo NPs (24,8 emu/g) (Table 1) and even larger than that of $CoFe_2O_4$ (29.7 emu/g) [27] – the spinel ferrite containing Fe and Co. This result indicates the improvement of $M_s$ of the synthesized core–shell NPs compared to various spinel ferrite-$SiO_2$ NPs [7,12,28]. With an increase of the $SiO_2$ thickness, the simultaneous decrease of both $M_S$ and $H_C$ values elucidates the change in the magnetic anisotropy of the $(FeCo)_x(SiO_2)_{100-x}$ NPs, which is a key parameter in the enhancement of SAR value [29,30]. Therefore, these results are decisive in understanding the influence of nonmagnetic shells on the magnetic induction heating (MIH) effect.

In order to investigate the effect of nonmagnetic $SiO_2$ shells on magnetic properties, we calculated the effective magnetic anisotropy ($K_{eff}$) of samples at $T = 5$ K and 300 K by the following equation:

$$K_{eff} = \frac{\mu_0 M_S H_C}{0.96} \quad (6)$$

where $\mu_0$ is the permeability of vacuum ($4\pi \times 10^{-7}$ H/m).

Table 2 represents calculated values of $K_{eff}$ which demonstrate its decrease with a growth of $SiO_2$ contribution both at 5 K and 300 K. Such behavior can be associated with the weakening of dipolar interaction between magnetic FeCo cores of × in $(FeCo)_x(SiO_2)_{100-x}$ NPs. As established in Fig. 2a, the average hydrodynamic size $d$ of $(FeCo)_x(SiO_2)_{100-x}$ NPs in an aqueous solution increases from 112 nm ($x = 90$) to 215 nm ($x = 70$). This obviously leads to the increase of the inter-particle distance and reduction of $K_{eff}$ value. This tendency well correlates with earlier presented in [31,32] observation that inter-particle distance is inversely proportional to blocking temperature $T_B$ for 5 nm and 7 nm $Fe_3O_4$ NPs. In accordance with the relationship $K_{eff} \cdot V \sim k_b \cdot T_B$, the observed in [32,33] reduction of $T_B$ value for $Fe_3O_4$ NPs of definite medium diameter is associated with the decrease of $K_{eff}$ due to the growth on the inter-particle distance [33]. Therefore, a simple model, which describes the relationship between $T_B$ and inter-particle distance proposed in [32], is also suitable for the consideration of the correlation between $K_{eff}$ and the thickness ($\delta$) of $SiO_2$ shells. We fitted these values (at 300 K) by the formula [34]:

**Table 2**
Values of A and B for $(FeCo)_x(SiO_2)_{100-x}$ NPs extracted by the fitting of equation (7): $D$ – medium diameter of FeCo core; $\bar{A}, \bar{B}$, $(\bar{A} + \bar{B})$ – medium values of fitted constants in the formula (6).

| $D$ (nm) | A·$10^4$ (erg/cm$^3$) | B·$10^4$ (erg/cm$^3$) | (A + B) ·$10^4$ (erg/cm$^3$) |
|---|---|---|---|
| 20 | 3.5 | 16.0 | 19.5 |
| 35 | 3.3 | 16.2 | 19.5 |
| 50 | 2.7 | 16.8 | 19.6 |
| | $\bar{A} = 3.2$ | $\bar{B} = 16.3$ | $\bar{(A+B)} = 19.5$ |

**Table 1**
Magnetic properties of $(FeCo)_x(SiO_2)_{100-x}$ ($70 \le x \le 90$, wt. %) NPs at $T = 5$ K and 300 K: $M_{H=5T}$ – magnetization at maximum applied magnetic field $H = 5$ T, $H_C$ – coercive force, $T_B$ – blocking temperature, $T_b$ – bifurcation temperature, $K_{eff}$ – magnetic anisotropy constant.

| Composition of $(FeCo)_x(SiO_2)_{100-x}$ | $M_{H=5T}$ (5 K) (emu/g) | $H_C$ (5 K) (Oe) | $K_{eff}$ ·$10^4$ (5 K) (erg/cm$^3$) | $M_{H=5T}$ (300 K) (emu/g) | $H_C$ (300 K) (Oe) | $K_{eff}$·$10^4$ (300 K) (erg/cm$^3$) | $T_B$ (K) | $T_b$ (K) |
|---|---|---|---|---|---|---|---|---|
| $x = 100$ | 63.5 | 387 | 1.3 | 24.8 | 90 | 19.5 | 150 | 283 |
| $x = 90$ | 47.7 | 325 | 0.5 | 38.0 | 154 | 4.9 | 138 | 297 |
| $x = 80$ | 37.5 | 268 | 0.4 | 27.3 | 113 | 3.7 | 161 | 295 |
| $x = 70$ | 19.1 | 262 | 0.1 | 11.8 | 112 | 2.1 | 170 | 286 |

$$K_{eff}(\delta) = A + \frac{B}{((D+2\delta)/D)^3} \quad (7)$$

where $A$ and $B$ are free parameters with the same unit as $K_{eff}$; $D$ is the medium diameter of NPs. Here, the value of $D+2\delta$ is the inter-nanoparticle distance between the core–shell $(FeCo)_x(SiO_2)_{100-x}$ NPs nanoparticles. Based on Eq. (7), the medium $(A+B)$ ($\sim 19.5 \cdot 10^4$ erg/cm$^3$) value is approximately equal to the value of $K_{eff}$ ($19.5 \cdot 10^4$ erg/cm$^3$) of FeCo NPs at $\delta = 0$. The $A$ value corresponds to the magnetic anisotropy of samples when the magnetic interaction between NPs is negligible ($\delta \gg D$). Presuming that the medium diameter of FeCo cores is in the range of 20–50 nm, we fitted all values of $K_{eff}$ for $(FeCo)_x(SiO_2)_{100-x}$ NPs series at $D_0 = 20, 35, 50$ nm. The fitted values of A and B are presented in Table 2.

### 3.3. Magnetic induction heating efficiency studies

The effect of $SiO_2$ shells on the magnetic induction heating efficiency of the $(FeCo)_x(SiO_2)_{100-x}$ NPs is investigated by the time-dependent heating curves $T(t)$ of the magnetic fluids containing NPs. Experiments are performed in alternating magnetic fields (AMF) with strength $H_{AC}$ in the range of 150–300 Oe and a frequency of 340 kHz. Correspondent $T(t)$ curves are shown in Fig. 5. The obtained $SAR_{exp}$ values of all samples at different amplitudes of the applied field $H_{AC}$ are shown in Fig. 6. It can be seen that the heating generation of the core–shell $(FeCo)_x(SiO_2)_{100-x}$ NPs depends strongly on the applied field amplitude as well as the thickness of $SiO_2$. SAR values for all samples almost linearly increase with the $H_{AC}$ value. This tendency is in good agreement with previous results [33,35].

As can be seen in Fig. 6, the highest value of $SAR_{exp}$ for all applied magnetic fields $H_{AC}$ is achieved for $(FeCo)_{80}(SiO_2)_{20}$ NPs. Interestingly, the existence of optimal thickness δ is also observed in experimental data at various $H_{AC}$. To explore the enhancement in SAR of the $(FeCo)_{80}(SiO_2)_{20}$ NPs compared to other compositions as well as the effect of $SiO_2$ shells in the heating property of the core–shell NPs, the role of each mechanism is elucidated [36].

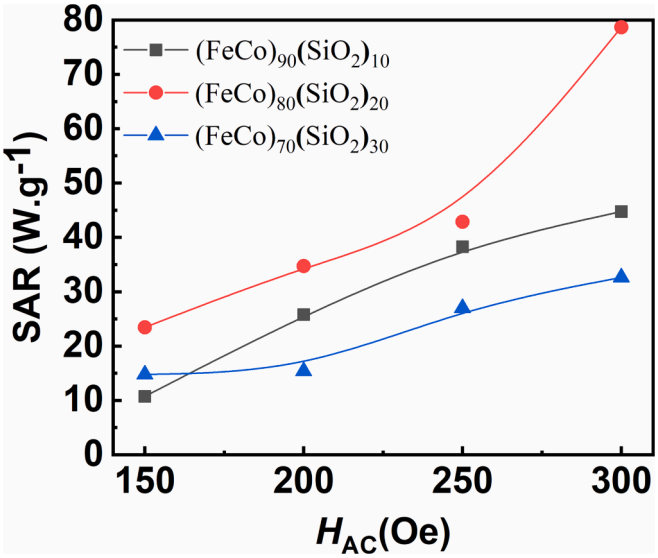


**Fig. 6.** The dependency of specific absorption rate ($SAR_{exp}$) on the applied magnetic field $H_{AC}$ the for $(FeCo)_x(SiO_2)_{100-x}$ NPs.

In general, the heating generation of the magnetic nanoparticles in AMF is contributed by three main loss mechanisms [37]: i) Neel relaxation losses; ii) Brown relaxation losses; iii) hysteresis losses. According to magnetic property results, all samples exhibit the interaction superparamagnetic behaviors at room temperature. It is well established that for superparamagnetic NPs, Neel and Brown relaxations dominate in heating efficiency. These relaxation mechanisms involve the rotation of the magnetic moments within each particle and the rotation of each particle itself in the fluids that directly relates to the intrinsic magnetic properties (magnetization and anisotropy energy) of NPs and their medium diameter [36].

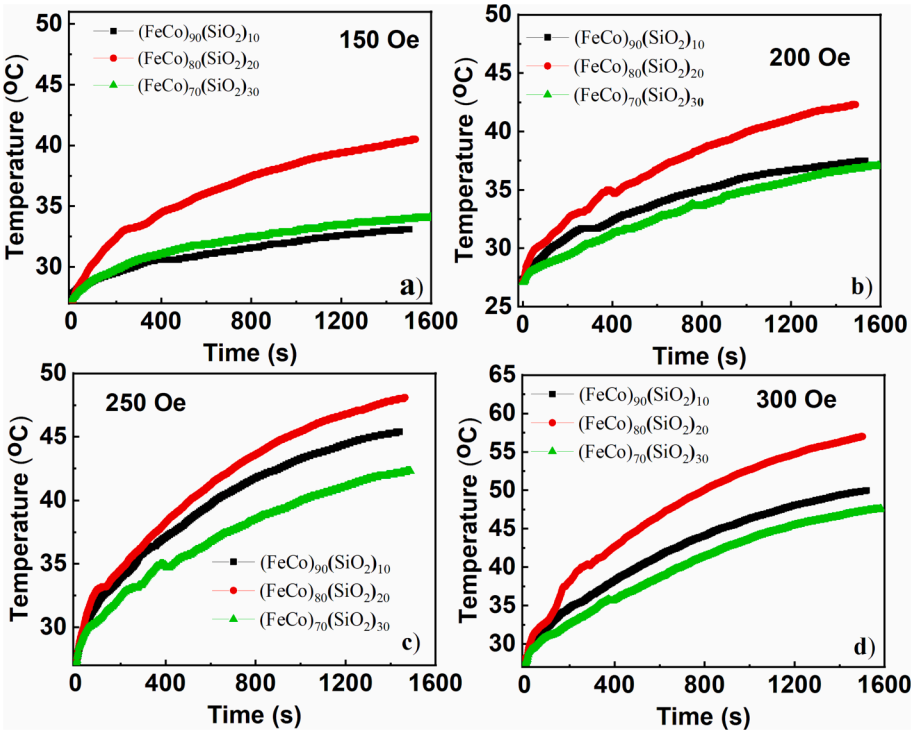


**Fig. 5.** Magnetic heating curves $T(t)$ of $(FeCo)_x(SiO_2)_{100-x}$ NPs under effect of magnetic field $H_{AC}$ with the amplitude 150 Oe (a), 200 Oe (b), 250 Oe (c), 300 Oe (d) and frequency of 340 kHz.

When magnetic NPs exhibit the interaction superparamagnetic behavior at room temperature, the total power density can be calculated by Linear Response Theory (LRT):

$$P^{LRT} = \pi\mu_0\chi'' H^2 f \tag{8}$$

in which, $\chi''$ is the imaginary susceptibility of NPs given by following equation:

$$\chi'' = \frac{2\pi f\tau}{1+(2\pi f\tau)^2}\chi_0 \tag{9}$$

where $\chi_0$ is the equilibrium susceptibility [35] and $\tau$ is the effective relaxation time given by:

$$\tau = \frac{\tau_N\tau_B}{\tau_N+\tau_B} \tag{10}$$

in which, $\tau_N$ and $\tau_B$ are Néel and Brown relaxation time, respectively. The Neel and Brown relaxation times were calculated by following equations:

$$\tau_N = \frac{\tau_0}{2}\sqrt{\frac{k_BT}{KV}}\exp^{KV/kT} \tag{11}$$

$$\tau_B = \frac{3\eta V_H}{kT} \tag{12}$$

Here, $\tau_0 = 10^{-9}$ s; $\eta$ is viscosity of magnetic fluid; the hydrodynamic volume of NPs ($V_H$) including the coating shell is written as:

$$V_H = \frac{\pi}{6}(D+2\delta)^3 \tag{13}$$

where, $D$ and $\delta$ are diameter and the thickness of the shell of NPs.

For the samples studied in the present work, the appearance of coercive field $H_C$ with values close to the applied field $H_{AC}$, makes it necessary to consider the contribution of also the hysteresis mechanism in the heating properties. Here, the Stoner-Wohlfarth model-based theories (SWMBTs) are suitable to calculate the hysteresis loss power. The value of power can be calculated by equation [38,39]:

$$P^{hys} = (4\mu_0 M_S H_C)f \tag{14}$$

The value of $H_C$ for the case of randomly oriented NPs is described by the following equation [33]:

$$\mu_0 H_C = 0.48\mu_0 H_C(b-\kappa^n) \tag{15}$$

in which, $b = 0.9$, $n = 1$ and $H_C = (\frac{2K_{eff}}{\mu_0 M_S})$ is the coercive field.

Now, the total power is given as:

$$P = P^{LRT} + P^{hys} \tag{16}$$

In accordance with [33] the theoretical value of $SAR_{theor}$ was calculated as follows:

$$SAR_{theo} = \frac{P}{\rho\phi} \tag{17}$$

where $\phi$ is the volume fraction and $\rho$ is the mean mass density (g/m$^3$) of the NPs.

Firstly, we calculated the value of SAR by SWMBTs assuming the experimental data $M_{H=5T}$, $H_C$ and $K_{eff}$ extracted or calculated from $M(H)$ magnetization curves for $(FeCo)_x(SiO_2)_{100-x}$ NPs (see Table 1). Fig. 7a shows the dependencies $SAR^{hys}_{theo}$ originating from the hysteresis mechanism as a function of $H_{AC}$. It is seen in Fig. 7a, the value of $SAR^{hys}_{theo}$ for each sample does not depend on the value of $H_{AC}$ because of its low value (150–300 Oe). In addition, a decrease of $SAR^{hys}_{theo}$ is observed with an increase of $\times$ value because it correlates with the magnetic anisotropy of the samples. When the content of $SiO_2$ in $(FeCo)_x(SiO_2)_{100-x}$ NPs increased, the simultaneous decrease of $M_{H=5T}$ and $H_C$ reflects the decrease of $K_{eff}$ values, which is related to the reduction of the SAR values. Therefore, exactly $SiO_2$ shells are the main reason for the reduction of the contribution of hysteresis loss to SAR value. In addition, all values of $SAR^{hys}_{theo}$ of $(FeCo)_x(SiO_2)_{100-x}$ NPs are smaller than the value of $SAR_{exp}$ at various $H_{AC}$ (Figs. 6 and 7a). Therefore, the contribution of Neel and Brown relaxation losses play the dominating role in the total heating of NPs. Thus, we have also to evaluate the role of $SiO_2$ on the SAR value by LRT approach assuming the experimental data ($M_{H=5T}$, $H_C$ and $K_{eff}$) of $(FeCo)_x(SiO_2)_{100-x}$ NPs. So, the calculations of $SAR^{LRT}_{theo}$ assuming the function of $K_{eff}(\delta)$ from the Eq. (7) instead of the constant value of $K$ in Eqs. (7)–(10) were conducted based on Eqs. (8)–(13), and Eq. (17). Following these equations, the thickness of $SiO_2$ shells affects not only the Néel relaxation but also Brown relaxation. The average value of SAR was computed for FeCo magnetic cores of NPs with a range of diameter $D$ = 20–50 nm (Fig. 7b). Interestingly, Fig. 7b indicates that there is an optimal thickness $\delta$ = 70 nm that corresponds to the maximum on the plot of $SAR^{LRT}_{theo}$ versus thickness of shells. As previously established, with an increase of the $SiO_2$ content in $(FeCo)_x(SiO_2)_{100-x}$ NPs, the $K_{eff}$ value decreases because of the weakening dipole interparticle interactions. This led to the change of the Neel and Brown relaxation time, which related to the bell shape of the plot of $SAR^{LRT}_{theo}$ versus thickness δ. The highest value at $\delta$ = 70 nm, corresponds to the value of experimentally established hydrodynamic diameter in a range of 90–120 nm. The dependence on the $SiO_2$ thickness of SAR value indicated the role of magnetic anisotropy in enhancing the heating efficiency. This result is consistent with the previous study [30], magnetic anisotropy was the key parameter in order to optimize the SAR value.

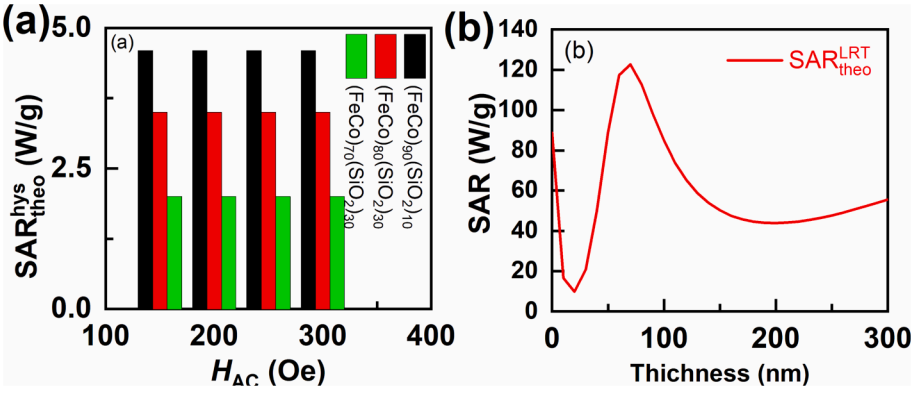


**Fig. 7.** The dependency of the $SAR^{hys}_{theo}$ on $H_{AC}$ for $(FeCo)_x(SiO_2)_{100-x}$ NPs (a), and the dependency of $SAR^{LRT}_{theo}$ on thickness of $SiO_2$ shells in $(FeCo)_x(SiO_2)_{100-x}$ NPs (b).

Based on the relationship between SAR and NPs concentration, L.T. Dat et. al observed the optimal concentration, which was explained by the effect of magnetic anisotropy on the SAR value of $Fe_3O_4$ NPs [34]. In particular, the magnetic anisotropy could be changed by varying the thickness of the shell for core–shell NPs or changing the concentration of magnetic fluids. These findings propose the approach to enhance the SAR value of magnetic fluids in hyperthermia.

It is worth noticing that, as indicated in Fig. 6, the highest SAR value is observed for $(FeCo)_{80}(SiO_2)_{20}$ NPs, whose hydrodynamic diameter is exactly about 150 nm, which is close to the theoretical value of optimal thickness. Also, $(FeCo)_{80}(SiO_2)_{20}$ NPs reveal the closed monodispersity. Therefore, obtained experimental data well correlates with the theoretical tendencies considered within the frame of LRT approach. These results also confirm that the main contribution of heating of $(FeCo)_x(SiO_2)_{100-x}$ NPs was due to Neel and Brown relaxation losses. All results indicate that the role of $SiO_2$ thickness δ in MIH effect is governed by the strength of dipole interactions between NPs magnetic cores as well as the value of their magnetic anisotropy.

### 3.4. Drug loading capacity studies

The results of fluorescent (FL) illustrating the drug-loading capacity of $(FeCo)_x(SiO_2)_{100-x}$ NPs are presented in Fig. 8. From the FL spectra of the free DOX in the solution, the DLE and DLC values of the core–shell $(FeCo)_x(SiO_2)_{100-x}$ NPs were calculated and listed in Table 3. It is seen that all samples exhibit excellent adsorption properties for loading DOX with DLE > 99 % and DLC ≥ 9 % for all samples. To confirm the DOX successfully loaded onto the $(FeCo)_x(SiO_2)_{100-x}$ NPs, the FTIR spectra of $(FeCo)_{70}(SiO_2)_{30}$ NPs (which sample shows the best DOX absorption capacity) before and after the drug loading experiment was studied and shown in Figure S2. FTIR spectra of both samples show the bands corresponding to the characterization vibration modes of $SiO_2$ and FeCo NPs. The bands with peaks at 477 $cm^{-1}$, 806.47 $cm^{-1}$ and 1041.26 $cm^{-1}$ could be assigned with the vibration of the Si-O bonds and the Si-O-Si bonds [40,41]. The bands with peak at 680 cm-1 could be attributed to the vibration mode of the metal (Fe and Co)-O bonds. A closer observation of the low-wave number range of the FTIR spectrum of the $(FeCo)_{70}(SiO_2)_{30}$ NPs after the drug loading experiment reveals the existence of the characteristic bands of DOX with peaks at 1579 $cm^{-1}$, 1420 $cm^{-1}$, 1211 $m^{-1}$, 1153 $cm^{-1}$ and 1083 $cm^{-1}$ [42]. This definitely confirms the successful loading of DOX onto the $(FeCo)_{70}(SiO_2)_{30}$ NPs.

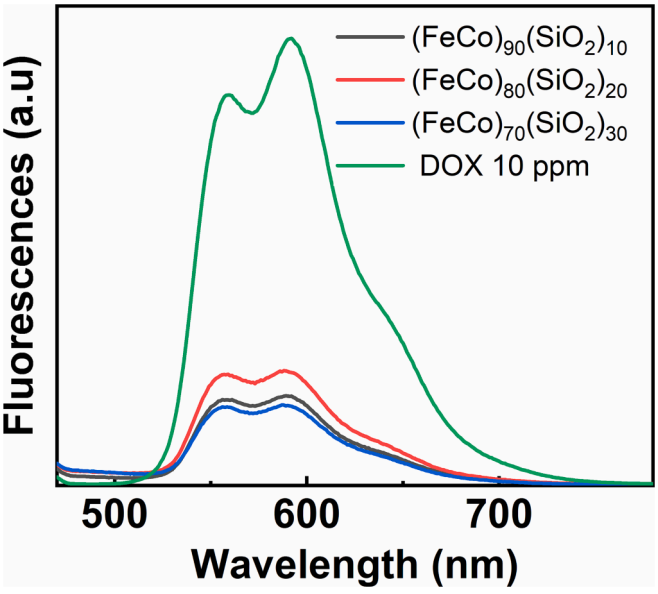


**Fig. 8.** Fluorescence spectra of free DOX in the solution after drug loading experiments for $(FeCo)_x(SiO_2)_{100-x}$ NPs.

**Table 3**
The values of drug loading efficiency (DLE), drug loading capacity (DLC) and Brunauer Emmett Teller (BET) surface area for $(FeCo)_x(SiO_2)_{100-x}$ NPs.

| Composition of $(FeCo)_x(SiO_2)_{100-x}$ NPs | DLE (%) | DLC (mg/g) | BET surface area ($m^2$/g) |
|---|---|---|---|
| $x = 90$ | 99.15 | 9.03 | 150.4 |
| $x = 80$ | 98.88 | 9.00 | 145.2 |
| $x = 70$ | 99.26 | 9.02 | 248.2 |

Additionally, the obtained results from Table 3 reveal that the DLC of the $(FeCo)_x(SiO_2)_{100-x}$ NPs is affected by the $SiO_2$ shell contribution. The highest DLC value was achieved for the $(FeCo)_x(SiO_2)_{100-x}$ sample with × = 70 and lower with × = 80 and 90. Noticeably, the specific surface area of the drug loading carries is an important factor that determines the drug loading capacity. The $N_2$ adsorption/desorption measurements were conducted to more explore the specific surface area of $(FeCo)_x(SiO_2)_{100-x}$ NPs with different $SiO_2$ shells ratios and are presented in Figure S3. All the samples exhibit type IV isotherms with a hysteresis loop belonging to the mesoporous structure. It can be seen that the core–shell $(FeCo)_x(SiO_2)_{100-x}$ NPs display a large specific surface area which is an advanced feature permitting a larger amount of DOX molecular easily accumulate on their surface. The obtained BET values for all samples (see Table 3) are in agreement with the drug loading results with the following $SiO_2$ contribution order: 30 wt% > 10 wt% > 20 wt %.

### 3.5. In vitro cytotoxicity

In order to apply the core–shell magnetic nanoparticles for biomedical therapy, it is necessary to evaluate their cytotoxicity. The cancer cells were chosen because of their sensitivity. The in vitro cytotoxicity effects of the core–shell $(FeCo)_x(SiO_2)_{100-x}$ NPs were against HepG2 cells, a human liver cancer cell line by means of SRB assay. Fig. 9 shows the cytotoxicity results of HepG2 cells treated with various concentrations of the core–shell $(FeCo)_x(SiO_2)_{100-x}$ NPs and DOX. After 48 h of incubation with the $(FeCo)_x(SiO_2)_{100-x}$ NPs, HepG2 cells showed excellent viability with cells living almost 100 % at dosage in the range of 31.25 to 60.25 μg/ml for all the samples, confirming the low concentration of NPs did not affect the cell survival. The IC50 values were estimated for the $(FeCo)_x(SiO_2)_{100-x}$ NPs with × = 90, 80 and 70 to be 457.2 ± 14.8 μg/ml, 209.9 ± 16.7 μg/ml, 699.1 ± 11.4 μg/ml, respectively. By comparison with the pure DOX, it can be seen that HepG2 cells died even at 3 μg/ml dosage of DOX which is significantly lower than the dosage of the $(FeCo)_x(SiO_2)_{100-x}$ NPs. Compared with toxicity results on the naked magnetic NPs reported in previous studies, it can be seen that the toxicity properties are significantly improved after coating with $SiO_2$ layers [43,44].

The viability of HepG2 cells can be assessed visually by observing their optical micrographs. Fig. 10 shows optical microscope images of HepG2 control cells and HepG2cells treated with $(FeCo)_{70}(SiO_2)_{30}$ NPs at concentrations of 31.25 μ/ml and 1000 μg/ml and doxorubicin. It can be seen that after 48 h, the HepG2 control cells (Fig. 10a) and HepG2 treated with $(FeCo)_{70}(SiO_2)_{30}$ NPs at a concentration of 31.25 μg/ml (Fig. 10b) spread to the plate and firmly adhere to the bottom, indicating good vitality. In contrast, HepG2 cells treated with the $(FeCo)_{70}(SiO_2)_{30}$ NPs at a concentration of 1000 μg/ml (Fig. 10c) and doxorubicin at a concentration of 31.25 μg/ml are round and some have fragmented cell membranes, almost no characteristic adhesion morphology can be observed.

## 4. Conclusion

The core–shell NPs of $(Fe_{25}Co_{75})_x(SiO_2)_{100-x}$ ($x = 70, 80, 90, 100$, wt. %) composition are successfully sintered by co-precipitation of FeCo cores from aqua solutions followed by deposition of $SiO_2$ shells by TEOS

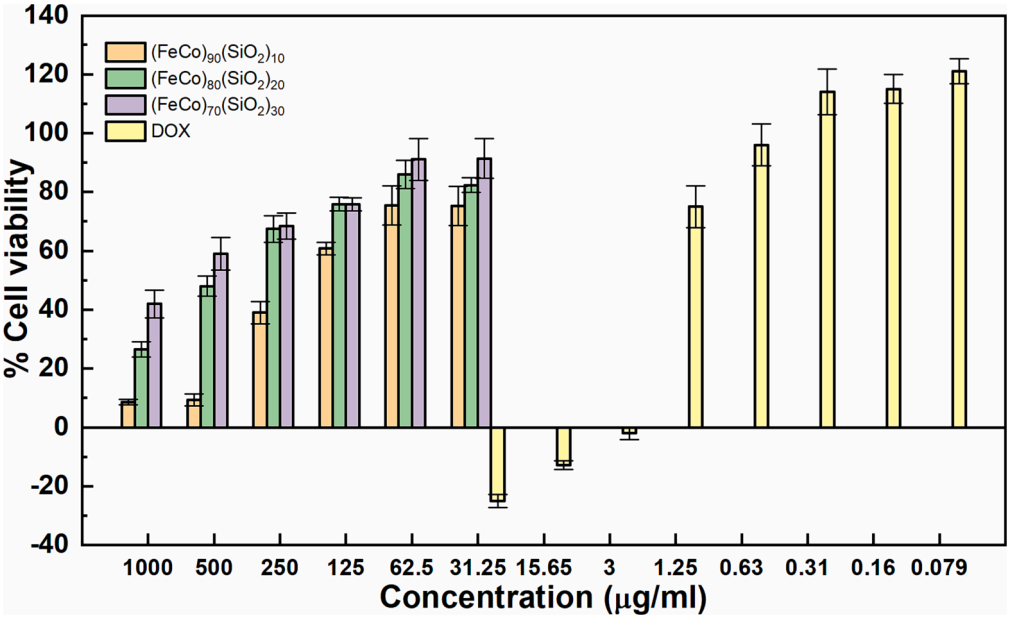


**Fig. 9.** Cell viability of HepG2 cells after treated with different concentrations of $(FeCo)_x(SiO_2)_{100-x}$ NPs ($x$ = 90, 80, 70).

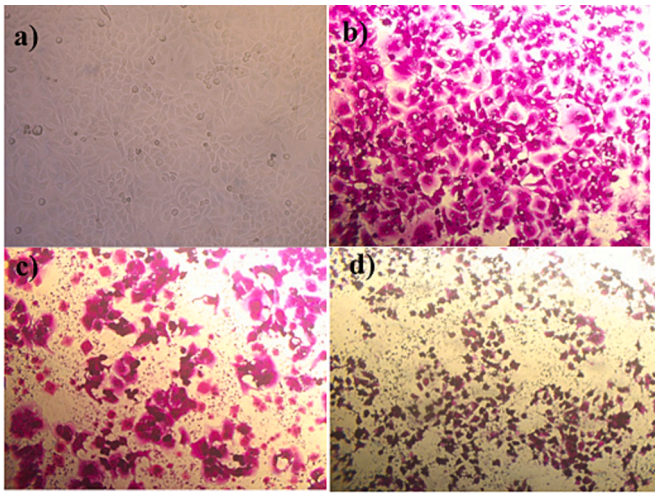


**Fig. 10.** Optical microscope images of HepG2 cells: control a); treated with $(FeCo)_{70}(SiO_2)_{30}$ NPs at concentration of 31.25 μg/ml (b), 1000 μg/ml (c) and doxorubicin (d) for 48 h.

hydrolysis. Study of the morphology, structure and phase composition of $(Fe_{25}Co_{75})_x(SiO_2)_{100-x}$ NPs proves the formation of the nearly spherical core–shell structures with medium diameter from 80 nm to 220 nm containing 20–50 nm cores of α-FeCo bcc alloy covered with amorphous $SiO_2$ shells. Mössbauer spectra evidence that the coverage with $SiO_2$ shells promotes the enhanced resistance of FeCo cores to surface oxidation. The observed simultaneous decrease of both $M_S$ and $H_C$ values when increasing $SiO_2$ contribution reflects falling magnetic anisotropy $K_{eff}$ value with growing $SiO_2$ shell thickness associated with the weakening of inter-particle interactions. As a consequence, the Linear Response Theory and Stoner-Wohlfarth model-based theories were applied to explore the induction magnetic heating of the samples. Neel and Brown relaxation losses are proved to be the main contributions to the heating dissipation of $(FeCo)_x(SiO_2)_{100-x}$ NPs that directly related to the thickness of $SiO_2$ shells, the strength of dipole inter-particle interactions and the magnetic anisotropy $K_{eff}$. From the semi-empirical calculation results of the heat capacity, the optimal $SiO_2$ shell thickness with the highest SAR values for their hyperthermia potential were released. The $SiO_2$ shell thickness (δ about 70 nm) well correlates with the hydrodynamic diameter ($d$ about 150 nm) for $(FeCo)_{80}(SiO_2)_{20}$ NPs experimentally demonstrating the highest SAR value. Sintered $(FeCo)_x(SiO_2)_{100-x}$ NPs in the whole composition range show high values of DOX drug loading efficiency and good compatibility with the HeG2 cells. Therefore, obtained $(FeCo)_x(SiO_2)_{100-x}$ NPs could be further applied for designing biocompatible nanodevices for effective application in theranostics.

## Declaration of Competing Interest

The authors declare that they have no known competing financial interests or personal relationships that could have appeared to influence the work reported in this paper.

## Data availability

Data will be made available on request.

*Acknowledgments*

Financial support of BRFFR-VANT project F21V-008 is gratefully acknowledged.

This work was also supported by funding from Viet Nam Academy of Science and Technology with a Grant number QTBY01.05/21-22 and from the Vietnamese Ministry of Science and Technology (MOST) under Project NĐT/BY/22/16.

The research was also supported by the subsidy of the Ministry of Education and Science (Poland) for the Lublin University of Technology as funds allocated for scientific activities in the scientific discipline of Automation, Electronics, Electrical Engineering and Space Technologies – grants: FD-20/EE-2/703, FD-20/EE-2/709.

## Appendix A. Supplementary material

Supplementary data to this article can be found online at https://doi.org/10.1016/j.mseb.2023.116571.

## References


[1] A. Shokuhfar, S. Salman, S. Afghahi, The heating effect of iron-cobalt magnetic nanofluids in an alternating magnetic field: application in magnetic hyperthermia treatment, Nanoscale Res. Lett. 8 (2013) 540, https://doi.org/10.1186/1556-276X-8-540.

[2] A. Zelenakova, V. Zelenak, I. Mat'ko, M. Strecˇkov, P. Hrubovc, J. Kovac, Superferromagnetism in chain-like Fe@SiO2 nanoparticle ensembles, J. Appl. Phys., 116 (2014) 033907. https://doi.org/10.1063/1.4890354.

[3] L.-M. Lacroix, R.B. Malaki, J. Carrey, S. Lachaize, M. Respaud, G.F. Goya, B. Chaudret, Magnetic hyperthermia in single-domain monodisperse FeCo nanoparticles: Evidences for Stoner-Wohlfarth behavior and large losses, J. Appl. Phys. 105 (2009), 023911, https://doi.org/10.1063/1.3068195.

[4] S. Moradi, O. Akhavan, A. Tayyebi, R. Rahighi, M. Mohammadzadeh, H.R.S. Rad, Magnetite/dextran-functionalized graphene oxide nanosheets for in vivo positive contrast magnetic resonance imaging, RSC. Adv. 5 (2015) 47529–47537, https://doi.org/10.1039/C5RA03331D.

[5] P.B. Kharat, S.B. Somvanshi, P.P. Khirade, K.M. Jadhav, Induction heating analysis of surface-functionalized nanoscale $CoFe_2O_4$ for magnetic fluid hyperthermia toward noninvasive cancer treatment, ACS Omega 5 (2020) 23378–23384, https://doi.org/10.1021/acsomega.0c03332.

[6] M.J. Hajipour, O. Akhavan, A. Meidanchi, S. Laurente, M. Mahmoudi, Hyperthermiainduced protein corona improves the therapeutic effects of zinc ferrite spinel-graphene sheets against cancer, RSC. Adv 4 (2014) 62557–62565, https://doi.org/10.1039/C4RA10862K.

[7] T.h. Dippong, E.A. Levei, I.G. Deac, F. Goga, O. Cadar, Investigation of structural and magnetic properties of $Ni_xZn_{1-x}Fe_2O_4/SiO_2$ ($0 \leq x \leq 1$) spinel-based nanocomposites, J. Anal. Appl. Pyrolysis. 144 (2019) 104713–104714, https://doi.org/10.1016/j.jaap.2019.104713.

[8] J. Alonso, H. Khurshid, V. Sankar, Z. Nemati, M.H. Phan, E. Garayo, J.A. García, H. Srikanth, FeCo nanowires with enhanced heating powers and controllable dimensions for magnetic hyperthermia, J. Appl. Phys. 117 (2015) 17D113, https://doi.org/10.1063/1.4908300.

[9] T.N. Kołtunowicz, P. Zukowski, J. Sidorenko, V. Bayev, J.A. Fedotova, M. Opielak, A. Marczuk, Ferromagnetic resonance spectroscopy of CoFeZr-$Al_2O_3$ granular films containing "FeCo core – oxide shell" nanoparticles, J. Magn. Magn. Mater. 421 (2016) 98–102, https://doi.org/10.1016/j.jmmm.2016.08.016.

[10] S. Jafari, H. Derakhshankhah, L. Alaei, A. Fattahi, B.S. Varnamkhasti, A. A. Saboury, Mesoporous silica nanoparticles for therapeutic/diagnostic applications, Biomed. Pharmacother. 109 (2019) 1100–1111, https://doi.org/10.1016/j.biopha.2018.10.167.

[11] T. Dippong, E.A. Levei, O. Cadar, I.G. Deac, M. Lazar, G. Borodi, I. Petean, Effect of amorphous $SiO_2$ matrix on structural and magnetic properties of $Cu_{0.6}Co_{0.4}Fe_2O_4/SiO_2$ nanocomposites, J. Alloys Compd 849 (2020), 156695, https://doi.org/10.1016/j.jallcom.2020.156695.

[12] T. Dippong, I.G. Deac, O. Cadar, E.A. Levei, Effect of Silica Embedding on the Structure, Morphology and Magnetic Behavior of $(Zn_{0.6}Mn_{0.4}Fe_2O_4)\delta/(SiO_2)(100-\delta)$ Nanoparticles, Nanomaterials 11 (2021) 2232, https://doi.org/10.3390/nano11092232.

[13] H. Das, N. Debnath, T. Arai, T. Kawaguchi, N. Sakamoto, K. Shinozaki, H. Suzuki, N. Wakiya, Superparamagnetic magnesium ferrite/silica core-shell nanospheres: A controllable $SiO_2$ coating process for potential magnetic hyperthermia application, Adv. Powder. Technol. 30 (2019) 3171–3181, https://doi.org/10.1016/j.apt.2019.09.026.

[14] M. Talaei, S.A. Hassanzadeh-Tabrizi, A. Saffar-Teluri, Synthesis of mesoporous $CuFe_2O_4@SiO_2$ core-shell nanocomposite for simultaneous drug release and hyperthermia applications, Ceram. Int. 47 (2021) 30287–30297, https://doi.org/10.1016/j.ceramint.2021.07.209.

[15] M. Tajabadi, I. Rahmani, S.M. Mirkazemi, H.G. Orimi, Insights into the synthesis optimization of Fe@ $SiO_2$ Core-Shell nanostructure as a highly efficient nano-heater for magnetic hyperthermia treatment, Adv. Powder. Technol. 33 (2022), 103366, https://doi.org/10.1016/j.apt.2021.11.018.

[16] F. Yang, H. Chen, D. Liu, P. Xiong, W. Li, X. Chen, The microstructure and magnetic properties of $FeCo@SiO_2$ core-shell nanoparticles synthesized by using a solution method, J. Alloys Compd. 728 (2017) 1153–1156, https://doi.org/10.1016/j.jallcom.2017.09.126.

[17] H. Ahmed, S.S. Gomte, E. Prathyusha, A. Prabakaran, A. Mukta, A. Amit, Biomedical applications of mesoporous silica nanoparticles as a drug delivery carrier, J. Drug. Deliv. Sci. Technol 76 (2022) 103729–103740, https://doi.org/10.1016/j.jddst.2022.103729.

[18] M.E. Peralta, S.A. Jadhav, G. Magnacca, D. Scalarone, D.O. Martire, M.E. Parolo, L. Carlos, Synthesis and in vitro testing of thermoresponsive polymer-grafted core-shell magnetic mesoporous silica nanoparticles for efficient controlled and targeted drug delivery, J. Colloid Interface Sci. 544 (2019) 198–205, https://doi.org/10.1016/j.jcis.2019.02.086.

[19] J. Fedotova, Local atomic order, morphology, and magnetic properties in silica-coated FeCo nanoparticles synthesized by coprecipitation technique, Phys. Status. Solidi B 259 (2022) 2100653–2100657, https://doi.org/10.1002/pssb.202100653.

[20] J.V. Kasiuk, J.A. Fedotova, T.N. Koltunowicz, P. Zukowski, A.M. Saad, J. Przewoznik, Cz. Kapusta, J. Zukrowski, I.A. Svito, Correlation between local Fe states and magnetoresistivity in granular films containing FeCoZr nanoparticles embedded into oxygen-free dielectric matrix, J. Alloys Compd., 586 (2014) S432–S435. https://doi.org/10.1016/j.jallcom.2012.09.058.

[21] K. Lagarec, D.G. Rancourt, Recoil User Manual - Mossbauer spectral analysis software for Windows, University of Ottawa, Ottawa, Canada, Department of Physics, 1998.

[22] P.H. Linh, N.V. Chien, D.D. Dung, P.H. Nam, D.T. Hoa, N.T.N. Anh, L.V. Hong, N. X. Phuc, P.T. Phong, Biocompatible nanoclusters of O-carboxymethyl chitosan-coated $Fe_3O_4$ nanoparticles: synthesis, characterization and magnetic heating efficiency, J. Mater. Sci. 53 (2018) 887–8900, https://doi.org/10.1007/s10853-018-2180-0.

[23] M. Gaumet, A. Vargas, R. Gurny, F. Delie, Nanoparticles for drug delivery: The need for precision in reporting particle size parameters, Eur. J. Pharm. Biopharm 69 (2008) 1–9. http://www/doi.org/10.1016/j.ejpb.2007.08.001.

[24] R.J. Pollard, C.M. Cardile, D.G. Lewist, L.J. Brown, Characterization of FeOOH polymorphs and ferrihydrite using low-temperature, applied-field, Mossbauer spectroscopy, Clay Minerals 27 (1992) 57–71, https://doi.org/10.1180/claymin.1992.027.1.06.

[25] T.h. Dippong, E.A. Levei, L. Diamandescu, I. Bibicu, C. Leostean, G.h. Borodi, L. B. Tudoran, Structural and magnetic properties of $Co_xFe_{3-x}O_4$ versus Co/Fe molar ratio, J. Magn. Magn. Mater. 394 (2015) 111–116, https://doi.org/10.1016/j.jmmm.2015.06.055.

[26] M. Suzuki, S.I. Fullem, I.S. Suzuki, L. Wang, C.J. Zhong, Observation of superspin-glass behavior in $Fe_3O_4$ nanoparticles, Phys. Rev. B 79 (2009), 024418, https://doi.org/10.1103/PhysRevB.79.024418.

[27] T. Dippong, E.A. Levei, O. Cadar, Investigation of Structural, Morphological and Magnetic Properties of $MFe_2O_4$ (M = Co, Ni, Zn, Cu, Mn) Obtained by Thermal Decomposition, Int. J. Mol. Sci. 23 (2022) 8483, https://doi.org/10.3390/ijms23158483.

[28] T. Dippong, E.A. Levei, C. Tanaselia, M. Gabor, M. Nasui, L.B. Tudoran, G. Borodi, Magnetic properties evolution of the $Co_xFe_{3-x}O_4/SiO_2$ system due to advanced thermal treatment at 700 °C and 1000 °C, J. Magn. Magn. Mater. 410 (2016) 47–54, https://doi.org/10.1016/j.jmmm.2016.03.020.

[29] I.M. Obaidat, B. Issa, Y. Haik, Magnetic properties of magnetic nanoparticles for efficient hyperthermia, Nanomaterials 5 (2015) 63–89, https://doi.org/10.3390/nano5010063.

[30] L.H. Nguyen, P.T. Phong, P.H. Nam, D.H. Manh, N.T.K. Thanh, L.D. Tung, N. X. Phuc, The Role of Anisotropy in Distinguishing Domination of Néel or Brownian Relaxation Contribution to Magnetic Inductive Heating: Orientations for Biomedical Applications, Materials 14 (2021) 1875, https://doi.org/10.3390/ma14081875.

[31] T.N. Lan, T.H. Hai, Monte Carlo simulation of magnetic nanoparticle systems, Comput. Mater. Sci. 49 (2010) S287–S290, https://doi.org/10.1016/j.commatsci.2010.01.025.

[32] C.J. Bae, S. Angappane, J.-G. Park, Y. Lee, J. Lee, K. An, T. Hyeon, Experimental studies of strong dipolar interparticle interaction in monodisperse $Fe_3O_4$ nanoparticles, Appl. Phys. Lett. 91 (2007) 102502–102503, https://doi.org/10.1063/1.2778758.

[33] P.T. Phong, L.H. Nguyen, I.J. Lee, N.X. Phuc, Computer Simulations of Contributions of Néel and Brown Relaxation to Specific Loss Power of Magnetic Fluids in Hyperthermia, J. Electron. Mater. 46 (2017) 2393–2405, https://doi.org/10.1007/s11664-017-5302-6.

[34] L.T. Dat, L.H. Nguyen, N.H. Nam, T.D. Van, L.T. Tam, N.X. Truong, V.Q. Nguyen, P. P. Thanh, P.H. Nam, Dependence of specific absorption rate on concentration of $Fe_3O_4$ nanoparticles: from the prediction of Monte Carlo simulations to experimental results, J. Nanopart. Res 24 (2022) 214, https://doi.org/10.1007/s11051-022-05596-z.

[35] S. Maenosono, S. Saita, Theoretical assessment of FePt nanoparticles as heating elements for magnetic hyperthermia, IEEE Trans. Magn. 42 (2006) 1638–1642.

[36] R.E. Rosensweig, Heating magnetic fluid with alternating magnetic field, J. Magn. Magn. Mater. 252 (2002) 370–374, https://doi.org/10.1016/S0304-8853(02)00706-0.

[37] Alison E. Deatsch, Benjamin. A. Evans, Heating efficiency in magnetic nanoparticle hyperthermia, J. Magn. Magn. Mater., 354 (2014) 163-172. https://doi.org/10.1016/j.jmmm.2013.11.006.

[38] J. Carrey, B. Mehdaoui, M. Respaud, Simple models for dynamic hysteresis loop calculations of magnetic single-domain nanoparticles: Application to magnetic hyperthermia optimization, J. Appl. Phys., 109 (2011) 083921-083921-083921-083917. https://doi.org/10.1063/1.3551582.

[39] L.H. Nguyen, V.T.K. Oanh, P.H. Nam, D.H. Doan, N.X. Truong, N.X. Ca, P.T. Phong, L.V. Hong, T.D. Lam, Increase of magnetic hyperthermia efficiency due to optimal size of particles: theoretical and experimental results, J. Nanoparticle Res. 22 (2020) 258 (216), https://doi.org/10.1007/s11051-020-04986-5.

[40] L. Zhao, X. Guo, Y. Liu, C. Ge, L. Guo, X. Shuc, J. Liu, Synergistic effects of silica nanoparticles/polycarboxylate superplasticizer modified graphene oxide on mechanical behavior and hydration process of cement composites, RSC Adv. 7 (2017) 16688–16702, https://doi.org/10.1039/C7RA01716B.

[41] J.-J. Liao, P.-Z. Gao, L. Xu, J. Feng, A study of morphological properties of $SiO_2$ aerogels obtained at different temperatures, J. Adv. Ceram. 7 (4) (2018) 307–316, https://doi.org/10.1007/s40145-018-0280-6.

[42] L. Chen, Y. Xue, X.Y. Xia, M. Song, J. Huang, H. Zhang, B. Yu, S. Long, Y. Liu, L. Liu, S. Huang, F. Yu, A redox stimuli-responsive superparamagnetic nanogel with chemically anchored DOX for enhanced anticancer efficacy and low systemic adverse effects, J. Mater. Chem. B 3 (2015) 8949–8962, https://doi.org/10.1039/C5TB01851J.

[43] S.P. Sherlock, S.M. Tabakman, L. Xie, H. Dai, Photothermally Enhanced Drug Delivery by Ultrasmall Multifunctional FeCo/Graphitic Shell Nanocrystals, ACS Nano 5 (2011) 1505–1512, https://doi.org/10.1021/nn103415x.

[44] S.P. Sherlock, H. Dai, Multifunctional FeCo-graphitic carbon nanocrystals for combined imaging, drug delivery and tumor-specific photothermal therapy in mice, Nano Res. 4 (2011) 1248–1260, https://doi.org/10.1007/s12274-011-0176-z.